The Astrophysical Journal Letters, 1008:L19 (12pp), 2026 September 1 https://doi.org/10.3847/2041-8213/ae946e

Expanding Magnetic Canopy Structure and Parasitic Polarities in a Quiet-Sun Network Element Observed by SUNRISE III/SCIP

Ryan J. Campbell[1], Carlos Quintero Noda[2,3], Mihalis Mathioudakis[1], Manuel Collados[2,3], Jack McFall[1], David B. Jess[1], Sami K. Solanki[4], Andreas Lagg[4], Achim Gandorfer[4], Jose Carlos del Toro Iniesta[5,6], Yukio Katsukawa[7,8,9], Pietro Bernasconi[10], Thomas Berkefeld[11], Alex Feller[4], Tino L. Riethmüller[4], Alberto Álvarez-Herrero[6,12], Masahito Kubo[7,9], H. N. Smitha[4], David Orozco Suárez[5,6], Bianca Grauf[4], Michael Carpenter[10], Alexander Bell[11], Valentín Martínez Pillet[2,6], Francisco Javier Bailén[5,6], Julian Blanco Rodríguez[6,13], Juan Sebastián Castellanos Durán[4], Edvarda Harnes[4], Johannes Hölken[4], Francisco A. Iglesias[4,14], Ryohtaroh T. Ishikawa[15], Yusuke Kawabata[7], Takuma Matsumoto[16], Takayoshi Oba[4,17], Azaymi L. Siu-Tapia[5,6], Hanna Strecker[5,6], Dušan Vukadinović[4,18], Hirohisa Hara[7], and Toshifumi Shimizu[19,20]

[1] Astrophysics Research Centre, Queen's University Belfast, Belfast, Northern Ireland, BT7 1NN, UK; ryan.campbell@qub.ac.uk
[2] Instituto de Astrofísica de Canarias, Vía Láctea, s/n, E-38205 La Laguna, Spain
[3] Departamento de Astrofísica, Universidad de La Laguna, E-38206 La Laguna, Tenerife, Spain
[4] Max-Planck-Institut für Sonnensystemforschung, Justus-von-Liebig-Weg 3, 37077, Göttingen, Germany
[5] Instituto de Astrofísica de Andalucía, CSIC, Glorieta de la Astronomía s/n, 18008 Granada, Spain
[6] Spanish Space Solar Physics Consortium, Spain
[7] National Astronomical Observatory of Japan, 2-21-1 Osawa, Mitaka, Tokyo 181-8588, Japan
[8] Department of Astronomy, The University of Tokyo, 7-3-1, Hongo, Bunkyo-ku, Tokyo 113-0033, Japan
[9] Department of Astronomical Science, The Graduate University for Advanced Studies (SOKENDAI), 2-21-1 Osawa, Mitaka, Tokyo 181-8588, Japan
[10] Johns Hopkins University Applied Physics Laboratory, 11100, Johns Hopkins Road, Laurel MD, USA
[11] Institut für Sonnenphysik (KIS), Georges-Köhler-Allee 401a, 79110 Freiburg, Germany
[12] Instituto Nacional de Técnica Aeroespacial (INTA), Ctra. de Ajalvir, km. 4, E-28850 Torrejón de Ardoz, Spain
[13] Universitat de Valencia Catedrático José Beltrán 2, E-46980 Paterna-Valencia, Spain
[14] Grupo de Estudios en Heliofísica de Mendoza, CONICET, Universidad de Mendoza, Boulogne sur Mer 683, 5500 Mendoza, Argentina
[15] National Institute for Fusion Science, 322-6 Oroshi-cho, Toki City 509-5292, Japan
[16] Center for Integrated Data Science, Institute for Space-Earth Environmental Research, Nagoya University, Furocho, Chikusa-ku, Nagoya, Aichi 464-8601, Japan
[17] Advanced Research Center for Space Science and Technology, Institute of Science and Engineering, Kanazawa University, Kakuma-machi, Kanazawa, Ishikawa 920-1192, Japan
[18] Institut für Physik, Universität Graz, Universitätsplatz 5, 8010 Graz, Austria
[19] Department of Earth and Planetary Science, The University of Tokyo, 7-3-1, Hongo, Bunkyo-ku, Tokyo 113-0033, Japan
[20] Institute of Space and Astronautical Science, Japan Aerospace Exploration Agency, 3-1-1, Yoshinodai, Chuo-ku, Sagamihara, Kanagawa 252-5210, Japan
Received 2026 July 3; revised 2026 August 3; accepted 2026 August 3; published 2026 August 27

Abstract

We present high-resolution multiline spectropolarimetric observations of a quiet-Sun network element obtained with the SUNRISE III Chromospheric Infrared SpectroPolarimeter. The observations combine photospheric, upper-photospheric, and chromospheric diagnostics at a spatial resolution and polarimetric sensitivity that allow the transverse magnetic structure of the network boundary to be examined directly. We find that the strongest linear polarization is concentrated in a narrow ridge around the edge of the magnetic element, cospatial with enhanced transverse magnetic field inferred from multiline inversions. The magnetic azimuth exhibits a coherent, predominantly radial organization around a more vertical core, consistent with an expanding magnetic canopy. An azimuth proxy derived directly from the observed Fe I and K I linear polarization reproduces the same large-scale organization, showing that this structure is encoded in the Stokes profiles rather than imposed by the inversion. Response functions and a MURaM-based forward-synthesis test indicate that the Fe I 8468 Å linear polarization is sensitive to magnetic azimuth in the upper photosphere, with the closest proxy agreement occurring near $\log \tau \approx -3$. We find no evidence for strong azimuthal shear between the Fe- and K-sensitive diagnostics. At the network boundary, we also identify localized parasitic-polarity patches associated with complex, multilobed Stokes V profiles and one case in which the Stokes V polarity reverses between photospheric Fe I and chromospheric Ca II lines. These results demonstrate that quiet-Sun network boundaries contain organized upper-photospheric canopy fields together with a small-scale mixed-polarity structure, providing new constraints on the three-dimensional magnetic structure of network elements.

Unified Astronomy Thesaurus concepts: Spectropolarimetry (1973); Quiet sun (1322); Quiet solar chromosphere (1986)

1. Introduction

Quiet-Sun magnetic fields are organized into a hierarchy of structures spanning from the weak internetwork to strong, concentrated magnetic elements in the network. These network fields, located at the boundaries of supergranular cells, are thought to play an important role in coupling the photosphere to the chromosphere and above (S. K. Solanki et al. 2006), but their resolved three-dimensional structure remains difficult to determine observationally (L. Bellot Rubio & D. Orozco Suárez 2019).

In photospheric layers, small magnetic concentrations are commonly associated with bright structures in intergranular lanes and magnetic bright points and are expected to evolve in geometry with height in a stratified atmosphere. Observational studies have provided evidence that such small-scale magnetic features expand and change their appearance between photospheric and higher-forming diagnostics, but detailed constraints on the vector magnetic field of resolved quiet-Sun network elements remain limited by the difficulty of measuring linear polarization signals in particular (M. J. Martínez González et al. 2012; P. H. Keys et al. 2019; C. Kuckein 2019). For example, M. J. Martínez González et al. (2012) inferred the expansion of a quiet-Sun network element indirectly from Stokes V asymmetries but could not recover its magnetic azimuth and could only weakly constrain its inclination.

Simultaneous multiline spectropolarimetry offers a promising route to solving this problem. In particular, the spectral region sampled by the Sunrise Chromospheric Infrared spectroPolarimeter (SCIP; Y. Katsukawa et al. 2026) on board the Sunrise III balloon-borne solar observatory (A. Korpi-Lagg et al. 2025) combines the photospheric Fe I 8514 Å, Fe I 8515 Å, and Fe I 8468 Å lines with the chromospheric Ca II 8498 Å and 8542 Å lines, providing sensitivity to both the photospheric and chromospheric magnetic fields (C. Quintero Noda et al. 2016). The K I D_1 7699 Å and K I D_2 7665 Å lines provide an additional sensitivity to magnetic field strength in the mid-to-upper photosphere (C. Quintero Noda et al. 2017). The Fe I 8468 Å line is especially valuable because of its strong sensitivity to the magnetic field vector, including enhanced sensitivity to the azimuth in the mid-to-upper photosphere compared with more commonly observed visible photospheric lines (C. Quintero Noda et al. 2021).

In this Letter, we use the unprecedented multiline capability of Sunrise III/SCIP to examine the magnetic structure of a quiet-Sun network element from the photosphere to the chromosphere. The key advance is the ability to combine high spatial resolution; sensitive polarimetry; and simultaneous Fe I, K I, and Ca II diagnostics in a quiet-Sun network region. This allows us to test for the first time whether the transverse field structure expected from an expanding canopy is directly recoverable in the observed linear polarization profiles and to search for small-scale mixed-polarity structures at the network boundary. To our knowledge, however, no previous observation has directly recovered the height-dependent vector structure of a quiet-Sun network canopy, including its internal azimuthal organization. For the first time, we are able to test whether that organization remains coherent with height or develops azimuthal shear. We show that the network element contains a coherent transverse field canopy surrounding a more vertical central region and that the inferred azimuthal organization is recovered independently from the observed linear polarization. Additionally, we find that localized parasitic polarity patches occur at the boundary, including one case showing opposite Stokes V polarity between photospheric and chromospheric diagnostics.

2. Observations

On 2024 July 11 between 04:28:47 and 06:15:55 UT, observations of a quiet-Sun region at disk center ($\mu = 1$) were obtained with the SCIP on board the Sunrise III balloon-borne solar observatory. The employed data were gathered as part of the observation with Sunrise ID: 04_QSUN (S. K. Solanki et al. 2026). The observations build on the heritage of earlier Sunrise flights and instrumentation (P. Barthol et al. 2011; S. K. Solanki et al. 2010, 2017). The flight took place under seeing-free conditions above the stratosphere. SCIP is a slit spectropolarimeter that scans in the direction perpendicular to the slit to build up two-dimensional maps of the solar surface. It operated in two spectral windows (SP1 and SP2), covering two spectral regions simultaneously. The spatial sampling along the slit and step size was 0$''$.094, with a total of 621 step positions, scanning a field of view of approximately 58$''$ × 58$''$.

The SP1 channel recorded a spectral region that includes the magnetically sensitive photospheric Fe I 8468 Å line, as well as Fe I 8514 Å and Fe I 8515 Å, and the chromospheric Ca II 8542 Å and 8498 Å lines, while the SP2 channel covered the K I D_1 and K I D_2 lines. The mean cadence between consecutive slit-step positions was 10.4 s. The standard deviation of the noise in the continuum regions of Stokes Q and V was $4.68 \times 10^{-4} I_c$ and $4.16 \times 10^{-4} I_c$, respectively, for SP1, where I_c is the spatially averaged continuum intensity.

In this Letter, we focus primarily on the analysis of the SP1 channel, specifically the Fe I 8468 Å, Fe I 8514 Å Fe I 8515 Å, Ca II 8498 Å, and Ca II 8542 Å lines, which together probe from the photosphere to the chromosphere. Where relevant, we incorporate the simultaneously observed K I D_1 and D_2 lines from the SP2 channel. We examine a network patch with significant linear and circular polarization signals. The internetwork regions are pervaded by both linear and circular polarization. In the Ca II lines, no linear polarization is measured, but significant circular polarization signals are detected in the network patches. Regions that are bright in the line core of the Fe I 8468 Å line are associated with the strongest magnetic concentrations. In the line core of the Ca II lines, one can observe chromospheric canopy structures (M. Kubo et al. 2026).

3. Multiline Inversions

After standard data reduction (S. K. Solanki et al. 2026), the full Stokes vector was inverted using the non–local thermodynamic equilibrium (NLTE) inversion code DESIRE (B. Ruiz Cobo et al. 2022). Photospheric Fe I lines were treated in LTE, while the K I and Ca II lines were treated in NLTE. Elemental abundances were adopted from M. Asplund et al. (2009). Each pixel was modeled with a single magnetic atmosphere characterized by stratified parameters including temperature, magnetic field strength, inclination, azimuth, and line-of-sight (LOS) velocity. The microturbulent velocity, $v_{\rm mic}$, was included as a free parameter with one node, while the macroturbulent velocity, $v_{\rm mac}$, was also a free parameter, primarily to account for the spectral point-spread function. Inversions were performed across the full field of view 10 times per pixel with varied initial conditions in B, γ, and ϕ, with the minimum χ^2 solution retained. The inversion was run through four cycles per pixel, with a final maximum number of nodes of nine in temperature and six in the other parameters. Earlier cycles used fewer nodes. The magnetic filling factor was fixed to unity. We focus our analysis on inversion-derived properties of a network patch exhibiting strong and spatially coherent polarization signals.

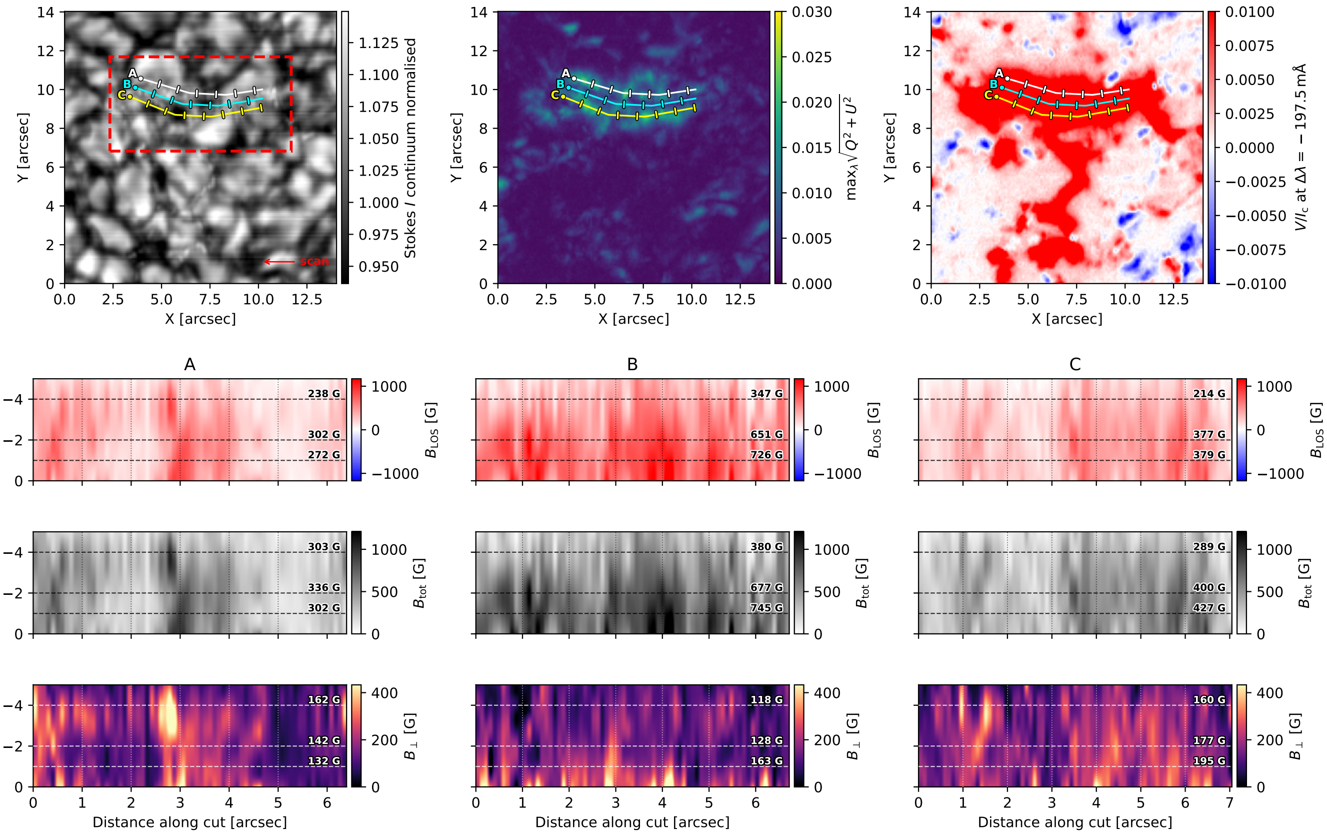

Figure 1. Overview of the analyzed network region and corresponding depth-dependent magnetic structure along three selected cuts. Top row: continuum intensity (left), maximum linear polarization signal $\max_\lambda \sqrt{Q^2+U^2}$ (middle), and Stokes V in the Fe I 8468 Å wing (right). Three spatial cuts (A, B, and C) tracing the linear polarization ridge are taken. Lower panels: stratifications along cuts A–C as a function of distance and optical depth $\log \tau$. Rows show LOS magnetic field $B_{\rm LOS}$, total field strength $B_{\rm tot}$, and transverse field component $B_\perp$, respectively. The dashed red box highlights the region shown in Figure 2. All Stokes quantities are continuum normalized. The tick marks on the upper panels and vertical lines on the lower panels denote 1″ increments. The median values at given optical depths are indicated on the bottom panels.

4. Magnetic Structure of the Network Element

4.1. Height-dependent Magnetic Field Properties

The continuum intensity map (Figure 1, top left) shows a granular field with bright structures in intergranular lanes associated with magnetic flux concentrations. The corresponding Stokes V map (Figure 1, top right) indicates that the region is primarily dominated by a single magnetic polarity, forming a spatially coherent patch. The maximum linear polarization signal, defined as $\max_\lambda \sqrt{Q^2(\lambda) + U^2(\lambda)}$ across the Fe I 8468 Å line (Figure 1, top middle), reveals an elongated ridge cospatial with the edge of the network element. This ridge or halo is not uniformly distributed across the magnetic patch but instead traces a confined structure offset from the center of the network element. Hereafter, we refer to the central region devoid of significant linear polarization as the "core" of the network element.

In order to examine the properties of the network structure, we describe the depth-dependent stratifications along three cuts labeled A–C. The cuts are intended to provide an illustrative example of the canopy structure, with the atmospheric quantities sampled along each path using bilinear interpolation. The exact placement of the cuts is not unique, but modest changes in their position or length do not alter the qualitative trends presented in this Letter. We show atmospheric parameters in this section from the inversions that included the simultaneously observed K I lines from the SP2 channel. The results in Figure 1 show that the LOS magnetic field, $B_{\rm LOS}$, remains consistently of one sign across the structure at photospheric depths ($\log \tau \sim 0$ to -2), with peak values exceeding ~kG in the core region (cut B). The total field strength $B_{\rm tot}$ has enhanced values concentrated in the central cut B and declines in cuts A and C. The $B_{\rm tot}$ and $B_{\rm LOS}$ both weaken in the chromosphere.

In contrast, the transverse component $B_\perp$ is enhanced along the same spatial locations as the linear polarization ridge, with increased horizontal field strengths in cuts A and C. This indicates that the magnetic field becomes more inclined in these regions. The ratio of the median transverse to median total field strengths, $\langle B_\perp \rangle / \langle B_{\rm tot} \rangle$, provides a representation for the characteristic field inclination along each cut. At $\log \tau = -1$, this behavior is reflected in median transverse-to-total field ratios of $\langle B_\perp \rangle / \langle B_{\rm tot} \rangle = 0.44$ and 0.46 for cuts A and C, respectively, compared to 0.22 for the central cut B, with corresponding median inclinations of 27° (A), 29° (C), and 14° (B). At $\log \tau = -2$, the contrast between the boundary and central cuts persists, with $\langle B_\perp \rangle / \langle B_{\rm tot} \rangle = 0.42$ (A), 0.44 (C), and 0.19 (B) and median inclinations of 27° (A), 29° (C), and 12° (B), respectively. This behavior persists into higher layers. At $\log \tau = -4$, all three cuts exhibit substantially larger median transverse-to-total field ratios than in the photosphere, indicating that the magnetic field becomes significantly more horizontal with height. Nevertheless, the boundary cuts continue to show larger $\langle B_\perp \rangle / \langle B_{\rm tot} \rangle$ values (≈0.54 (A), 0.55 (C), and 0.31 (B)).

4.2. Transverse Magnetic Field Structure

The large amount of linear polarization in the network region detected in Fe I 8468 Å enables us to investigate the spatial variation of the inferred magnetic azimuth across it. In fact, there is significant linear polarization detected in the K I 7699 Å line as well. For the avoidance of doubt, this analysis probes variations in field orientation in the plane of the solar surface. We conduct the analysis in this section with the inversion that includes the K lines. The upper panel of Figure 2 shows the continuum intensity in the region of strongest linear polarization, overlaid with a quiver representation of the magnetic azimuth inferred from the inversion. The vector lengths scale with the transverse magnetic field strength, $B_\perp$, emphasizing the locations where the transverse component is strongest. The enhanced transverse field is concentrated along the boundaries of the network element, while the interior remains comparatively vertical, forming a central core of weak $B_\perp$.

To assess whether the inferred azimuthal structure is present directly in the observations, we construct an azimuth proxy from the linear polarization. For each pixel, we compute wavelength-integrated Stokes parameters over the Fe I 8468 Å line,

$$Q_{\rm int}(x, y) = \sum_{\lambda_1}^{\lambda_2} Q(\lambda, x, y), \quad U_{\rm int}(x, y) = \sum_{\lambda_1}^{\lambda_2} U(\lambda, x, y), \tag{1}$$

and define the corresponding azimuth proxy as

$$\chi_{\rm LP}(x, y) = \frac{1}{2}\,{\rm atan2}(U_{\rm int}(x, y),\; Q_{\rm int}(x, y)), \tag{2}$$

which provides a formation-weighted estimate of the transverse field orientation, defined modulo 180°.[21] Figure 2 shows the azimuth proxy derived directly from the observed linear polarization. Without relying on any inversion assumptions, this proxy exhibits the same spatial organization as the inversion-derived azimuth. The magnetic azimuths exhibit a coherent radial pattern centered on the most vertical region of the network element. Moving away from this central core, the transverse field orientation varies systematically around the structure, consistent with an expanding magnetic canopy. At the periphery of the network element, neighboring regions often exhibit distinct azimuthal orientations, producing measurable lateral variations in the transverse field direction along the canopy boundary.

Panels (d) and (e) repeat this comparison using the K I D_1 7699 Å line. The K-proxy preserves the same large-scale azimuthal organization seen in Fe, and we find no evidence for a strong additional azimuthal shear between the Fe- and K-sensitive diagnostics within this network element; the azimuths from the two lines typically agree within 5°–10° of each other. This should not be interpreted as assigning either proxy to a single optical-depth layer; rather, both proxies represent contribution-weighted measurements of the emergent linear polarization.

[21] We note that in principle, integrating across the Stokes Q and U profiles may incur cancellations, but we ultimately find the proxy is useful as a sanity check on the inversion where the linear polarization signals are strong.

4.3. Comparison with MURaM Simulations

To qualitatively place the inferred magnetic structure in a broader physical context, we examined a representative quiet-Sun network element from a radiative magnetohydrodynamic (rMHD) simulation produced with MURaM (M. Rempel 2012). The illustrative simulation shown in Figure 3 was selected from the SPIN4D MURaM archive (K. E. Yang et al. 2024), specifically from the `SPIN4D_SSD_Large` case. This simulation spans a larger horizontal domain (50 × 50 Mm) than the other released cases while retaining the same high spatial resolution (16 km in the horizontal direction), allowing extended quiet-Sun network structures to develop self-consistently within realistic magnetoconvection. The selected network element was taken from a quadrant of the simulation containing relatively strong magnetic flux concentrations. The simulation therefore provides a physically plausible example of a mature quiet-Sun network concentration exhibiting organized transverse magnetic structure and spatially coherent azimuthal variation. While the comparison presented here is qualitative, the MURaM atmosphere offers a realistic magnetohydrodynamic context for interpreting the inferred morphology of the observed network element.

Figure 3 shows the photospheric temperature structure, the synthetic linear polarization signal computed over the Fe I 8468 Å spectral window, and the transverse magnetic field and azimuth at $\log \tau = -2$. The Fe I 8468 Å Stokes profiles were forward-synthesized from the MURaM atmosphere using DeSIRe in synthesis mode, allowing the spatial distribution of the synthetic linear polarization signatures to be compared qualitatively with the SCIP observations. The simulated network element exhibits several qualitative similarities to the SCIP observations. The magnetic structure is anchored in a cool, vertically dominated central core with comparatively weak transverse field and linear polarization signal, while enhanced linear polarization and transverse magnetic field occur preferentially around the boundary of the flux concentration. The inferred azimuthal structure is also spatially radial, with coherent lateral variation in field orientation around the network element.

An additional comparison is provided in the fourth panel of Figure 3, which shows the azimuth proxy derived directly from the synthesized Stokes Q and U signals using the same methodology applied to the SCIP observations. The proxy generally reproduces the large-scale organization of the underlying magnetic azimuth, including the radial structure around the flux concentration and the coherent lateral variations along its boundary. A pixel-by-pixel comparison yields a median absolute difference of 14°7 between the proxy and the ground-truth azimuth at $\log \tau = -2.9$. Although local discrepancies are present, the agreement demonstrates that the proxy retains substantial information on the underlying magnetic field orientation and is capable of recovering the dominant azimuthal morphology present in the simulation. The comparison also highlights the limitations of any azimuth diagnostic derived directly from observed linear polarization. Fine-scale variations visible in the simulation are partially suppressed or lost when the azimuth is inferred from the emergent Stokes signals. Degradation arising from finite spatial resolution, instrumental noise, and LOS averaging would further reduce the fidelity with which the underlying azimuthal structure can be recovered. Most importantly, this demonstrates the Fe I 8468 Å line has significant sensitivity to the transverse magnetic field orientation

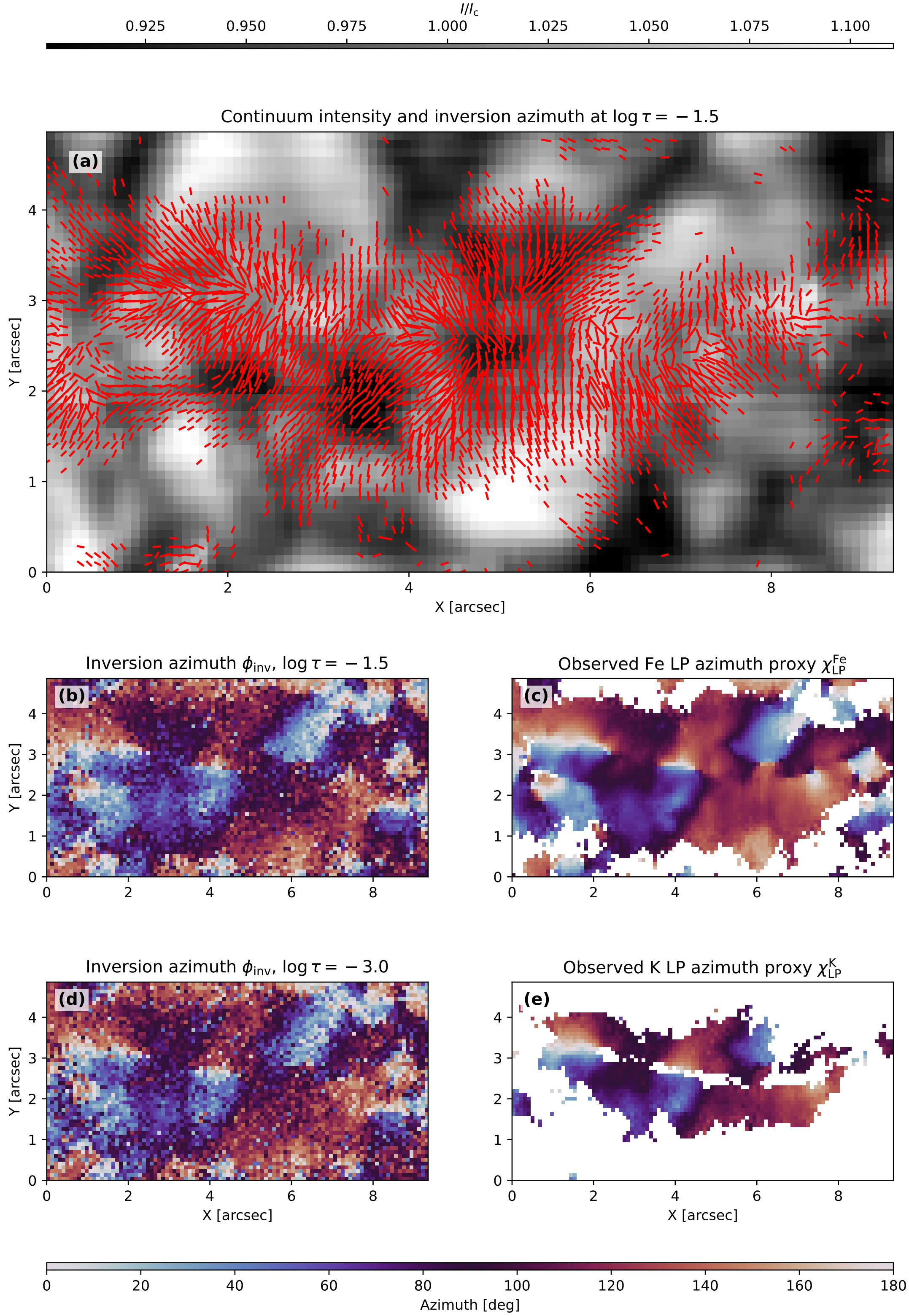

Figure 2. Transverse magnetic field structure of the network element in the region highlighted by the dashed red box in Figure 1. (a) The background shows the continuum intensity, while the red line segments indicate the corresponding magnetic azimuth, with lengths proportional to $B_\perp$. (b) Magnetic azimuth $\phi_{\rm inv}$ inferred from the inversion at $\log\tau = -1.5$. (c) Azimuth proxy $\chi_{\rm LP}$ derived directly from the observed linear polarization of the Fe I 8468 Å line. Panels (d) and (e) show the same as (b) and (c) but for $\log\tau = -3.0$ and the K I 7699 Å line. In the lower panels (b)-(e), pixels are masked unless the amplitude of either Stokes Q or U exceeds $5\sigma_{QU}$ at one or more wavelengths. The close correspondence between the inversion and the proxy shows that the lateral variation in field orientation is already present in the observed Stokes profiles.

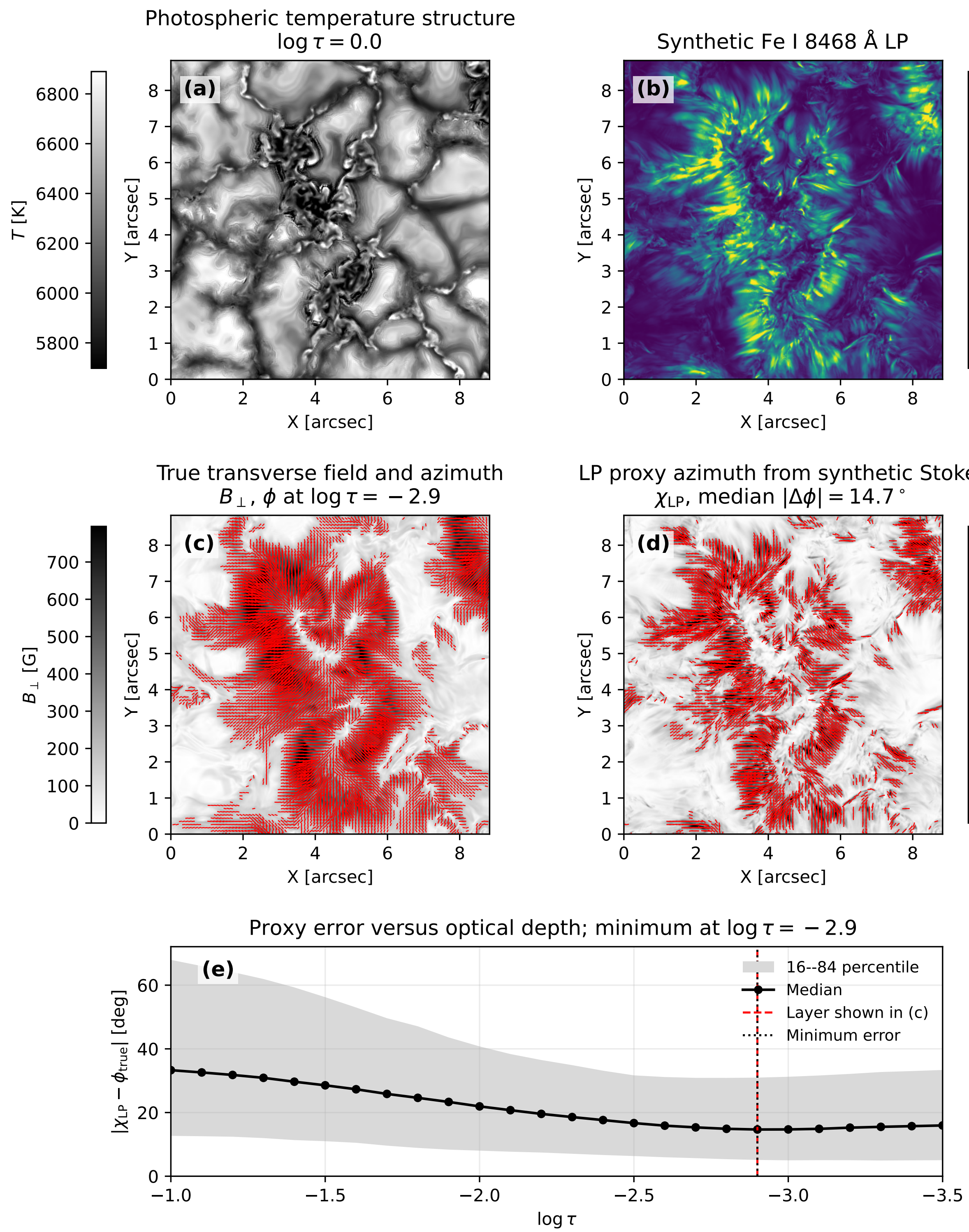

Figure 3. Illustrative magnetic structure of a quiet-Sun network element from a MURaM simulation. (a) Temperature at $\log \tau = 0$, showing a cool, concentrated magnetic core embedded within the granular photosphere. (b) Maximum linear polarization signal, $\max_\lambda \sqrt{Q^2 + U^2}$, computed over the synthetic Fe I 8468 Å spectral window. The strongest linear polarization occurs preferentially around the boundary of the magnetic concentration rather than within the central core. (c) Transverse magnetic field strength $B_\perp$ at $\log \tau = -2.9$, with red lines indicating the magnetic azimuth directions. (d) Azimuth proxy derived from the synthesized Stokes Q and U profiles using the same methodology applied to the SCIP observations, overlaid on the synthetic linear polarization map. Red lines indicate the inferred azimuth orientation. (e) Median absolute difference between the azimuth proxy, $\chi_{\rm LP}$, and the ground-truth magnetic azimuth in the MURaM simulation as a function of optical depth. The shaded region denotes the 16th–84th percentile range. The minimum error occurs near $\log \tau \approx -2.9$, indicating that the wavelength-integrated Fe I 8468 Å line is most sensitive to the magnetic azimuth at upper-photospheric heights.

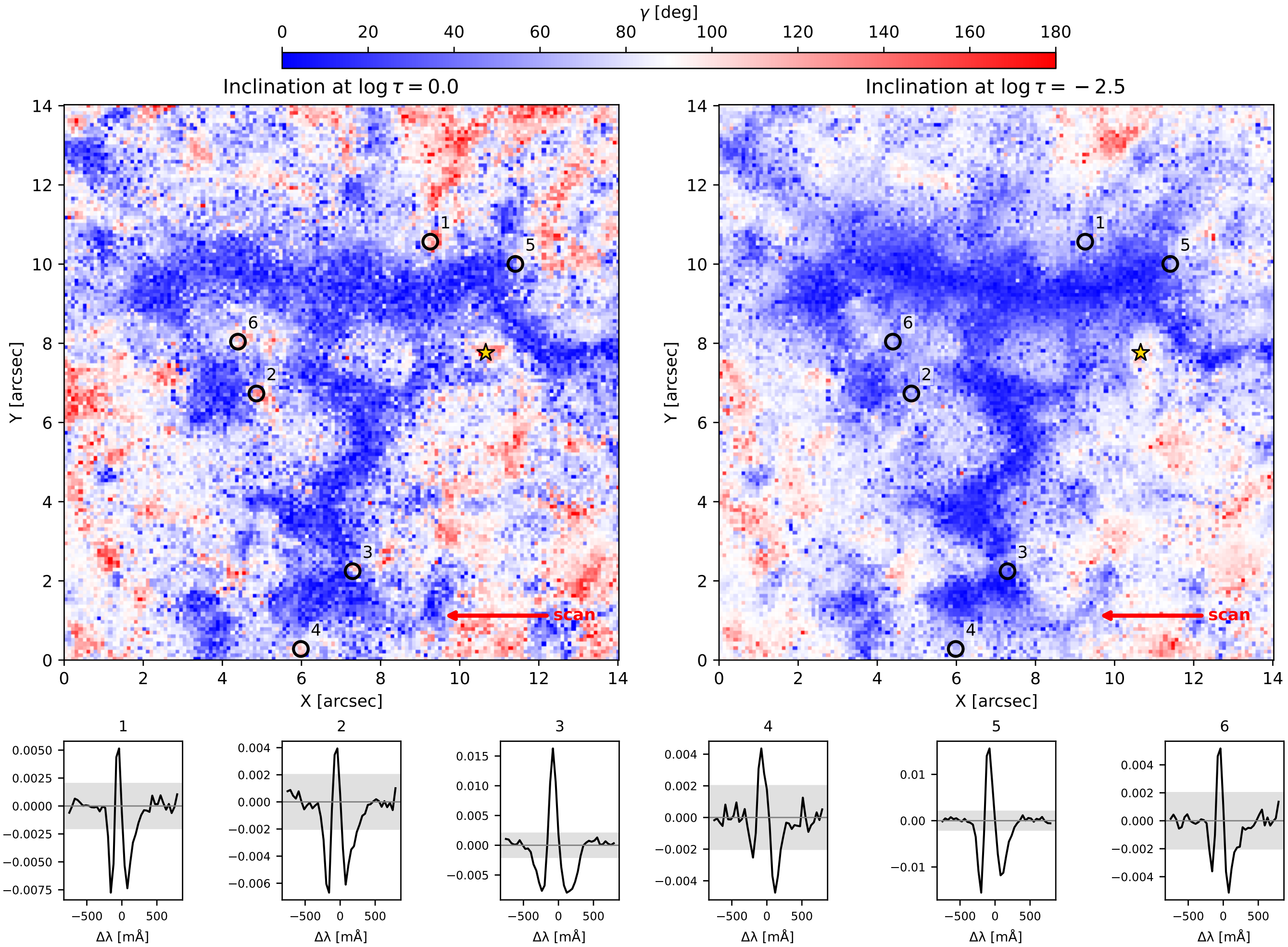

Figure 4. Magnetic field inclination in the network region at two representative photospheric depths. Top left: inclination γ at $\log \tau = 0$. Top right: inclination at $\log \tau = -2.5$. Black circles mark locations exhibiting three-lobed Stokes V profiles in the Fe I 8468 Å line, where the inferred polarity reverses between the two layers. Labels 1–6 correspond to the profile examples shown in the lower panels. The gold star marks a distinct location where the observed Stokes profiles show opposite polarity between the photospheric Fe and chromospheric Ca lines, shown in Figure 6. Bottom panels: example Stokes V profiles from the locations marked 1–6, illustrating the range of three-lobed morphologies observed at the network boundary. The shaded regions show the 5σ noise level.

in the upper photosphere. Appendix A shows this is consistent with the response functions.

4.4. Small-scale Parasitic Magnetism

Figure 4 reveals the presence of small-scale patches whose magnetic polarity reverses with height. These features appear as localized regions embedded within, or adjacent to, the dominant network field but exhibit opposite inclination between the two sampled layers. We refer to them here as parasitic patches. We conduct analysis on these with the inversion that did not include the K I lines.

The parasitic patches are preferentially located near the boundaries of the network element. Their spatial distribution is not uniform but instead confined to specific regions that also exhibit enhanced complexity in the Stokes profiles. As demonstrated by the lower panels in Figure 4, these locations are characterized by distinctly three-lobed Stokes V profiles, consistent with the presence of LOS gradients in the magnetic field strength, LOS velocity, or inclination (I. Rueedi et al. 1992; S. K. Solanki & C. A. P. Montavon 1993; C. Kiess et al. 2018; R. J. Campbell et al. 2023). The highlighted pixels are illustrative rather than being presented as an exhaustive list, as there are other parasitic polarity patches that are not highlighted. Further, other network patches in the region scanned by SCIP show these parasitic patches also, as demonstrated in Appendix B.

Figure 5 shows an example inversion result for one of the boundary pixels identified in Figure 4 as exhibiting a three-lobed Stokes V profile in the Fe I 8468 Å line. The observed and fitted Stokes profiles are shown together with the corresponding atmospheric stratification returned by the inversion. The inversion reproduces the asymmetric and multilobed Stokes V morphology in the Fe lines while maintaining comparatively simpler chromospheric Stokes V profiles in the Ca II lines. The inferred atmospheric stratification contains strong gradients in the magnetic and velocity parameters along the LOS, consistent with the interpretation discussed above. This figure is intended only as an illustrative example of the type of inversion solution associated with the parasitic boundary pixels.

4.5. Polarity Reversal between the Photosphere and Chromosphere

In the example shown in Figure 6, the Stokes V signals from the photospheric Fe I and chromospheric Ca II lines exhibit opposite signs. The location of this patch is shown by the star

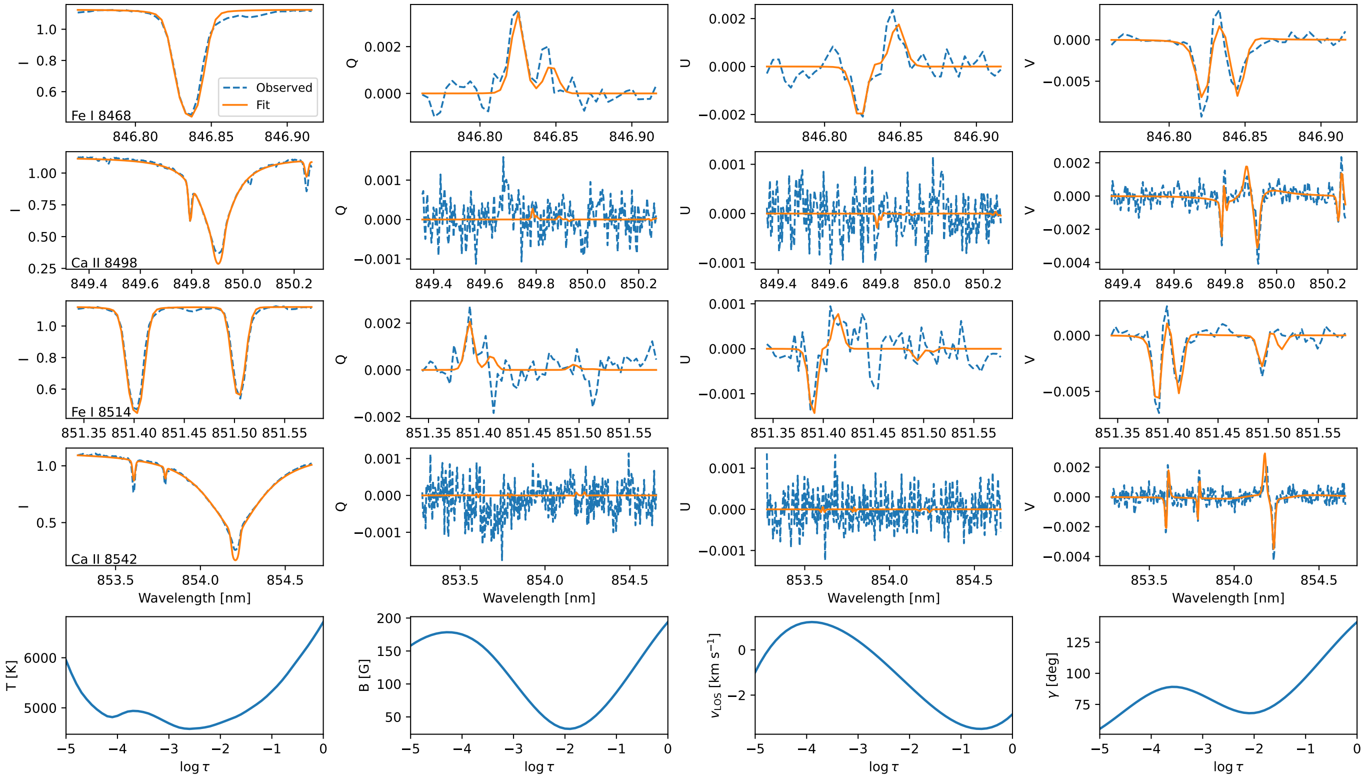

Figure 5. Example Stokes profile fits for a boundary pixel identified as exhibiting a three-lobed Stokes *V* profile in the Fe I 8468 Å line. The inversion reproduces the multilobed Stokes *V* signature in the Fe line, while the Ca lines remain two-lobed in Stokes *V*. The inferred stratification indicates that the observed asymmetry is consistent with strong LOS velocity (and magnetic) gradients.

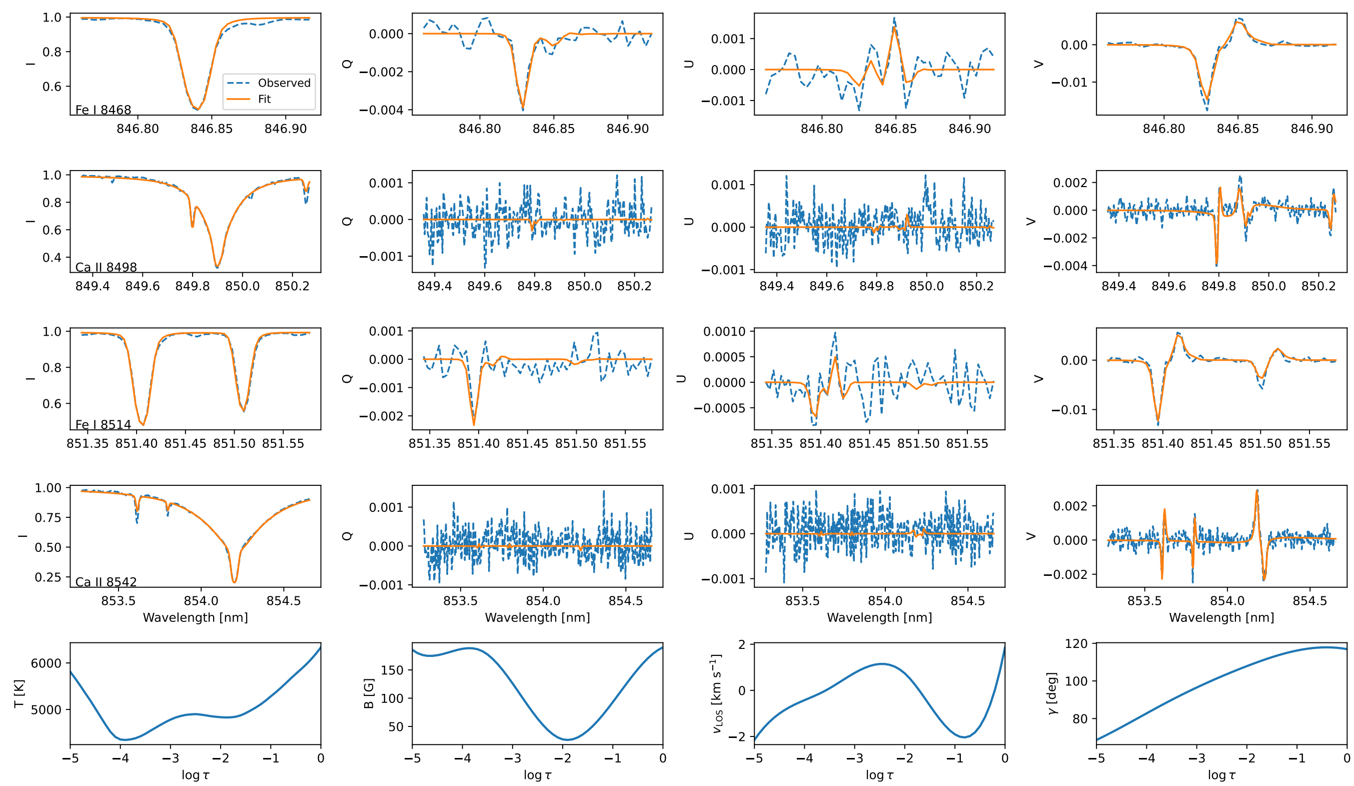

Figure 6. Example Stokes profile and inversion fits for the location marked by the star in Figure 4. Observed (dashed) and fitted (solid) Stokes profiles are shown for Fe I 8468 Å, Ca II 8498 Å, Fe I 8514 Å, Fe I 8515 Å, and Ca II 8542 Å. The Stokes *V* profiles exhibit opposite polarity between the photospheric Fe lines and the chromospheric Ca lines. The lower panels (bottom row) show the inferred atmospheric stratification as a function of optical depth, including the temperature, magnetic field strength, LOS velocity, magnetic inclination, and magnetic azimuth returned by the inversion.

marker in Figure 4. This behavior indicates a significant change in magnetic configuration with height and is not easily reproduced by a single, depth-independent magnetic field. This could arise as a result of an overlying canopy-like chromospheric field of opposite polarity to the underlying small-scale photospheric magnetic field. The Stokes V profiles are consistent over several pixels. While the profiles shown in Figures 4 and 6 represent individual pixels, they are representative of the types of Stokes V morphologies observed in the regions identified as parasitic in the inclination maps. Taken together, these diagnostics suggest that the parasitic patches are associated with a complex magnetic structure involving vertical gradients.

5. Discussion

A significant observational advance of this work is that the canopy-like transverse field structure is detected through the linear polarization of a quiet-Sun network element, rather than inferred only from Stokes V (M. J. Martínez González et al. 2012). Previous observations have established that the quiet-Sun network flux expands with height, but direct constraints on the resolved azimuthal organization of the associated transverse field have remained limited by weak linear polarization signals. The SCIP observations show a coherent boundary ridge of linear polarization, enhanced $B_\perp$, and a radial azimuthal pattern around a comparatively vertical core. This combination provides a direct magnetic view of the mid-to-upper-photospheric network canopy. The network magnetic field is found to be predominantly vertical in the photosphere, becoming progressively more inclined with height. The inferred morphology is qualitatively consistent with the magnetic expansion observed in larger solar magnetic structures, where comparatively vertical core fields are surrounded by progressively more inclined boundary fields and enhanced transverse magnetic components (e.g., S. K. Solanki & O. Steiner 1990; S. K. Solanki et al. 1999).

We also qualitatively compared the inferred magnetic morphology with a quiet-Sun network element from a MURaM simulation. We emphasize that this comparison is intended only as an illustrative physical context rather than a quantitative forward-modeling validation of the observations. Nevertheless, the simulation exhibits qualitatively similar organization of the transverse magnetic field and lateral azimuthal variation, indicating that the type of structured magnetic morphology inferred from the SCIP observations can arise naturally in realistic magnetoconvective network fields. Perhaps most surprisingly, the MURaM validation further suggests that the azimuthal information encoded in the emergent Fe I 8468 Å linear polarization is weighted toward considerably higher layers than would otherwise be assumed. In the simulation, the minimum median difference between the linear polarization azimuth proxy and the underlying magnetic azimuth occurs near $\log \tau \approx -3$. This result does not imply a single formation height for the line, but it suggests that interpretations of observed Fe I 8468 Å linear polarization solely in terms of lower-photospheric magnetic azimuth may overlook a significant contribution from upper-photospheric layers. The result may also help explain why the inclusion of the K I lines does not substantially alter the inferred azimuthal morphology of the network element, despite their expected sensitivity to higher atmospheric layers (C. Quintero Noda et al. 2017). This conclusion is also substantiated by the response functions shown in Appendix A.

In addition, we identify significant small-scale complexity at the boundaries of the network element. Localized, small-scale patches exhibiting three-lobed Stokes V profiles and opposite-polarity LOS fields indicate the presence of strong gradients or unresolved structure within the resolution element. In many cases, the inferred LOS magnetic field changes sign between photospheric depths. This is not unique to this network element, as other network elements in the SCIP field of view also show similar parasitic patches (see Appendix B). The presence of localized opposite-polarity features near network boundaries is perhaps related to previous observations of flux emergence and cancellation in quiet-Sun regions, where internetwork fields continuously interact with and modify the network flux (M. Gošić et al. 2014, 2016). Similar opposite-polarity features were reported by D. Buehler et al. (2015) in plage regions.

Meanwhile, we find a distinct example that shows opposite polarity between photospheric and chromospheric lines. Apparent polarity reversals between photospheric and chromospheric lines can arise from line formation effects, in particular, due to changes in the sign of $dI/d\lambda$ in the presence of line core emission (J. Sanchez Almeida 1997; M. Gošić et al. 2021). However, opposite-polarity Stokes V signals between Fe I and Ca II lines have also been reported and interpreted as signatures of height-dependent magnetic morphology in emerging magnetic structures (A. Sainz Dalda & A. López Ariste 2007). In the present case, the absence of emission features in the Ca II line cores and the inferred stratification are consistent with a genuine change, rather than an apparent change, in the direction of the magnetic field vector with height. In principle, this represents a possible site for magnetic reconnection. To our knowledge, this is the first detection of such a polarity reversal in a quiet-Sun network element, made possible by the high-resolution, multiline observations of Sunrise III/SCIP. Photosphere-chromosphere polarity reversals have also been observed by Sunrise III in flares (R. Ishikawa et al. 2026; C. Quintero Noda et al. 2026).

6. Conclusions

We have analyzed high-resolution multiline spectropolarimetric observations of a quiet-Sun network element obtained with Sunrise III/SCIP, combining photospheric and chromospheric diagnostics. Our main findings are as follows:

1. The network magnetic field is strongest and most vertical within the central core of the structure, becoming progressively more inclined with height and distance from the core.
2. The transverse magnetic field is enhanced along the boundaries of the network element, where the magnetic azimuth exhibits a predominantly radial organization centered on a strong, vertical magnetic core. This geometry is consistent with an expanding magnetic canopy.
3. Localized boundary pixels exhibit complex Stokes V profiles and opposite-polarity LOS fields, indicative of strong gradients or unresolved magnetic structure.
4. A distinct example shows opposite-sign Stokes V profiles between photospheric and chromospheric lines,

consistent with a height-dependent reversal of the LOS magnetic field.

5. A representative MURaM network element exhibits a similar radial organization of the magnetic field, with the enhanced transverse field surrounding a comparatively vertical core.
6. We do not detect any azimuthal shear along the LOS. However, the Fe I 8468 Å line is sensitive to the magnetic azimuth much higher in the atmosphere than other commonly observed photospheric spectral lines.

Taken together, these results indicate that the magnetic field within quiet-Sun network elements exhibits significant lateral and vertical structuring, particularly at the boundaries. Such complexity may play an important role in mediating energy transport in the lower solar atmosphere and underlines the importance of combining high spatial and spectral resolution with sensitive polarimetry.

Acknowledgments

R.J.C., M.M., and D.B.J. acknowledge support from the Science and Technology Facilities Council (STFC) under grant No. ST/X000923/1. Sunrise III is supported by funding from the Max-Planck-Förderstiftung (Max Planck Foundation), NASA under grants #80NSSC18K0934 and #80NSSC24M0024 (“Heliophysics Low Cost Access to Space” program), and the ISAS/JAXA Small Mission-of-Opportunity program and JSPS KAKENHI grant Nos. JP18H05234 and JP23K25916. This research has received financial support from the European Union’s Horizon 2020 research and innovation program under grant agreement No. 824135 (SOLARNET) and No. 101097844 (WINSUN) from the European Research Council (ERC). It has also been funded by the Deutsches Zentrum für Luft- und Raumfahrt e.V. (DLR, grant No. 50 OO 1608). The Spanish contributions have been funded by the Spanish MCIN/AEI under projects RTI2018-096886-B-C5, PID2021-125325OB-C5, and PID2024-156066OB-C5, and from “Center of Excellence Severo Ochoa” awards to IAA-CSIC (SEV-2017-0709, CEX2021-001131-S), all co-funded by European REDEF funds, “A way of making Europe.”

Data Availability Statement

The Sunrise observations are openly available via the Sunrise-3 Mission Archive (https://sr3data.mps.mpg.de).

Appendix A
Response Functions to Magnetic Azimuth

To investigate the atmospheric layers contributing to the observed azimuthal signatures, we computed response functions to perturbations in the magnetic azimuth using the DESIRE synthesis module. The calculations were performed using a semi-empirical quiet-Sun reference atmosphere with magnetic field strength $B = 500$ G, LOS velocity $v_{\mathrm{LOS}} = 0.5\,\mathrm{km\,s^{-1}}$, magnetic azimuth $\phi = 70^\circ$, and magnetic inclination $\gamma = 45^\circ$.

Figure 7 shows the wavelength-integrated response functions to magnetic azimuth for several commonly observed spectropolarimetric diagnostics. For each spectral line, the Stokes Q and U response functions were combined and integrated over the wavelength to provide a measure of the total sensitivity of the emergent linear polarization to perturbations in magnetic azimuth as a function of optical depth. Each curve was subsequently normalized to its peak value to facilitate comparison of the depth dependence.

The response functions demonstrate substantial differences in the atmospheric layers sampled by the various diagnostics. The K I D_1 and D_2 lines do exhibit sensitivity extending into higher layers than the visible Fe I lines at 5250 Å and 6302 Å. However, the Fe I 8468 Å line displays a notably extended response toward upper-photospheric layers. This behavior is consistent with the MURaM-based validation presented in Section 4.3, where the azimuth proxy derived from the Fe I 8468 Å linear polarization exhibited its closest correspondence to the underlying magnetic azimuth near $\log\tau \approx -3$.

These calculations do not imply that the Fe I 8468 Å line possesses a single formation height nor that the inferred azimuth proxy can be associated uniquely with a particular optical depth.

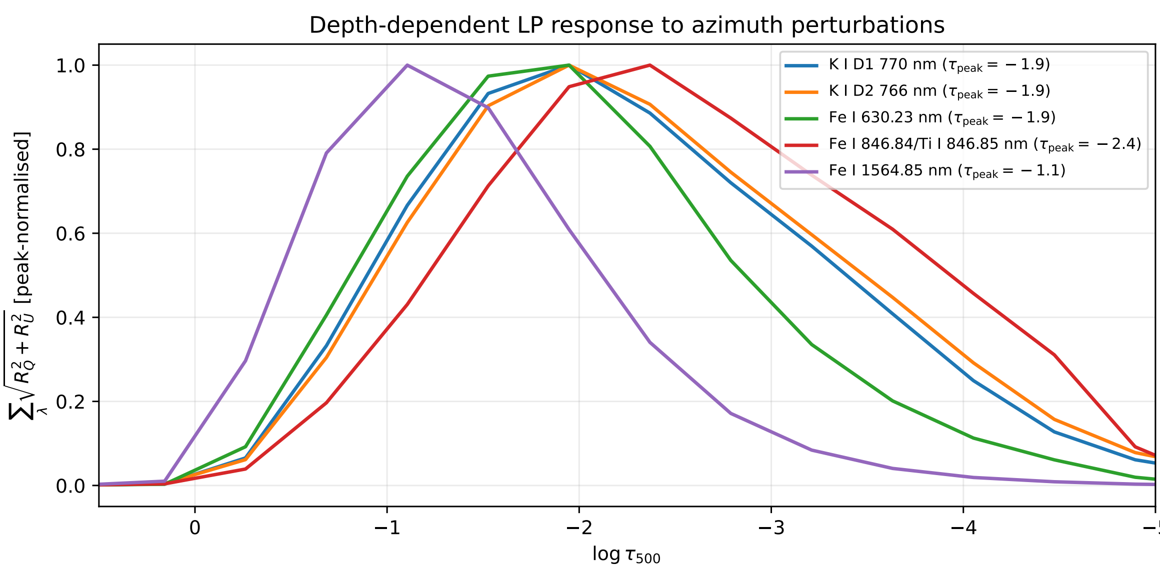

Figure 7. Normalized wavelength-integrated linear polarisation (LP) response functions to magnetic azimuth for selected spectropolarimetric diagnostics. For each line, the Stokes Q and U response functions were combined and integrated over wavelength before normalization. The Fe I 8468 Å line exhibits substantial sensitivity to upper-photospheric layers, extending to optical depths significantly higher than K I D_1 and D_2.

Nevertheless, they indicate that the linear polarization observed in this line retains significant sensitivity to upper-photospheric magnetic structure. Consequently, interpretations of Fe I 8468 Å azimuth measurements solely in terms of lower-photospheric magnetic fields may overlook an important and perhaps even dominant contribution from higher atmospheric layers.

Appendix B
Parasitic Polarity Patches in Other Network Elements

To assess whether the parasitic polarity patches identified in the primary network element are representative, we examined three additional network elements located elsewhere within the SCIP field of view, shown in Figure 8. All three additional examples exhibit compact magnetic concentrations accompanied by smaller-scale patches of contrasting magnetic inclination in their immediate surroundings. The opposite-polarity parasitic patches are visible at $\log \tau = 0$ and mostly vanish in the upper photosphere (as shown by the $\log \tau = -2.5$ map). These examples suggest that the mixed-polarity patches are not restricted to a single network element but are present in multiple magnetic concentrations across the observed quiet-Sun field. In Figure 8, the three additional network elements are labeled as regions of interest (ROIs) B, C, and D.

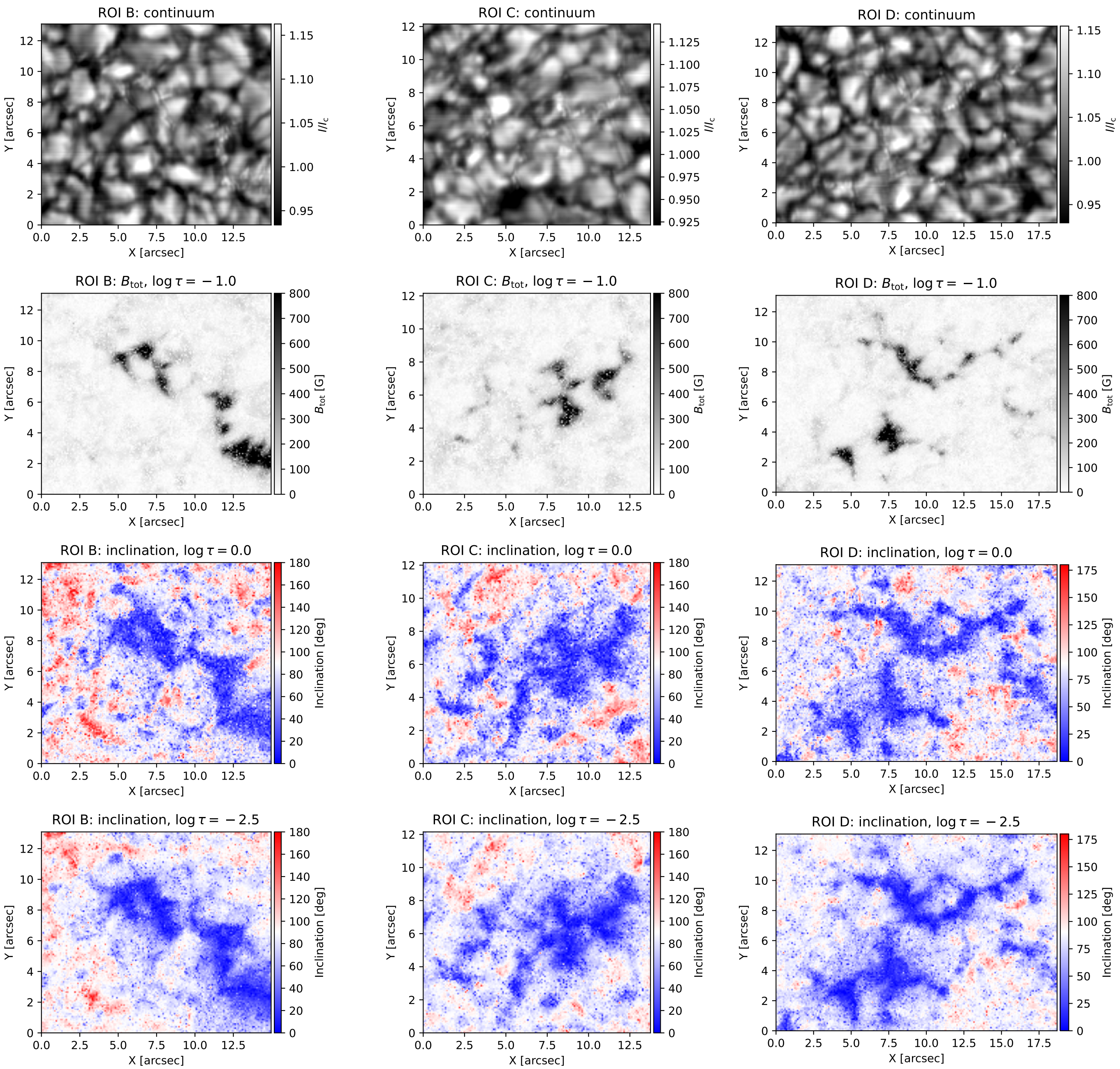

Figure 8. Additional examples of three quiet-Sun network elements identified within the SCIP field of view. The top row shows continuum intensity, the second row shows the inferred magnetic field strength, and the third and fourth rows show the magnetic inclination at $\log \tau = 0$ and $\log \tau = -2.5$, respectively. All quantities are derived from the multiline inversions. Similar to the network element analyzed in detail throughout this work, each region exhibits a compact magnetic concentration surrounded by smaller-scale patches of differing magnetic inclination.

ORCID iDs

Ryan J. Campbell https://orcid.org/0000-0001-5699-2991
Carlos Quintero Noda https://orcid.org/0000-0001-5518-8782
Mihalis Mathioudakis https://orcid.org/0000-0002-7725-6296
Manuel Collados https://orcid.org/0000-0002-6210-9648
Jack McFall https://orcid.org/0009-0009-9220-8231
David B. Jess https://orcid.org/0000-0002-9155-8039
Sami K. Solanki https://orcid.org/0000-0002-3418-8449
Andreas Lagg https://orcid.org/0000-0003-1459-7074
Achim Gandorfer https://orcid.org/0000-0002-9972-9840
Jose Carlos del Toro Iniesta https://orcid.org/0000-0002-3387-026X
Yukio Katsukawa https://orcid.org/0000-0002-5054-8782
Pietro Bernasconi https://orcid.org/0000-0002-0787-8954
Alex Feller https://orcid.org/0009-0009-4425-599X
Tino L. Riethmüller https://orcid.org/0000-0001-6317-4380
Alberto Álvarez-Herrero https://orcid.org/0000-0001-9228-3412
Masahito Kubo https://orcid.org/0000-0001-5616-2808
H. N. Smitha https://orcid.org/0000-0003-3490-6532
David Orozco Suárez https://orcid.org/0000-0001-8829-1938
Valentín Martínez Pillet https://orcid.org/0000-0001-7764-6895
Francisco Javier Bailén https://orcid.org/0000-0002-7318-3536
Julian Blanco Rodríguez https://orcid.org/0000-0002-2055-441X
Juan Sebastián Castellanos Durán https://orcid.org/0000-0003-4319-2009
Edvarda Harnes https://orcid.org/0009-0002-6808-5154
Johannes Hölken https://orcid.org/0000-0001-6029-7529
Francisco A. Iglesias https://orcid.org/0000-0003-1409-1145
Ryohtaroh T. Ishikawa https://orcid.org/0000-0002-4669-5376
Yusuke Kawabata https://orcid.org/0000-0001-7452-0656
Takuma Matsumoto https://orcid.org/0000-0002-1043-9944
Takayoshi Oba https://orcid.org/0000-0002-7044-6281
Azaymi L. Siu-Tapia https://orcid.org/0000-0003-0175-6232
Hanna Strecker https://orcid.org/0000-0003-1483-4535
Dušan Vukadinović https://orcid.org/0000-0003-1971-5551
Hirohisa Hara https://orcid.org/0000-0001-5686-3081
Toshifumi Shimizu https://orcid.org/0000-0003-4764-6856

References

Asplund, M., Grevesse, N., Sauval, A. J., & Scott, P. 2009, ARA&A, 47, 481
Barthol, P., Gandorfer, A., Solanki, S. K., et al. 2011, SoPh, 268, 1
Bellot Rubio, L., & Orozco Suárez, D. 2019, LRSP, 16, 1
Buehler, D., Lagg, A., Solanki, S. K., & van Noort, M. 2015, A&A, 576, A27
Campbell, R. J., Keys, P. H., Mathioudakis, M., et al. 2023, ApJL, 955, L36
Gošić, M., Bellot Rubio, L. R., del Toro Iniesta, J. C., Orozco Suárez, D., & Katsukawa, Y. 2016, ApJ, 820, 35
Gošić, M., Bellot Rubio, L. R., Orozco Suárez, D., Katsukawa, Y., & del Toro Iniesta, J. C. 2014, ApJ, 797, 49
Gošić, M., De Pontieu, B., Bellot Rubio, L. R., Sainz Dalda, A., & Pozuelo, S. E. 2021, ApJ, 911, 41
Ishikawa, R., Katsukawa, Y., Kubo, M., et al. 2026, ApJL, In press
Katsukawa, Y., del Toro Iniesta, J. C., Solanki, S. K., et al. 2026, SoPh, 301, 99
Keys, P. H., Reid, A., Mathioudakis, M., et al. 2019, MNRAS, 488, L53
Kiess, C., Borrero, J. M., & Schmidt, W. 2018, A&A, 616, A109
Korpi-Lagg, A., Gandorfer, A., Solanki, S. K., et al. 2025, SoPh, 300, 75
Kubo, M., Katsukawa, Y., Kawabata, Y., et al. 2026, arXiv:2607.26353
Kuckein, C. 2019, A&A, 630, A139
Martínez González, M. J., Bellot Rubio, L. R., Solanki, S. K., et al. 2012, ApJL, 758, L40
Quintero Noda, C., Barklem, P. S., Gafeira, R., et al. 2021, A&A, 652, A161
Quintero Noda, C., Ferrente, F., Katsukawa, Y., et al. 2026, ApJL, 1006, L46
Quintero Noda, C., Shimizu, T., de la Cruz Rodríguez, J., et al. 2016, MNRAS, 459, 3363
Quintero Noda, C., Uitenbroek, H., Katsukawa, Y., et al. 2017, MNRAS, 470, 1453
Rempel, M. 2012, ApJ, 750, 62
Rueedi, I., Solanki, S. K., Livingston, W., & Stenflo, J. O. 1992, A&A, 263, 323
Ruiz Cobo, B., Quintero Noda, C., Gafeira, R., et al. 2022, A&A, 660, A37
Sainz Dalda, A., & López Ariste, A. 2007, A&A, 469, 721
Sanchez Almeida, J. 1997, A&A, 324, 763
Solanki, S. K., Finsterle, W., Rüedi, I., & Livingston, W. 1999, A&A, 347, L27
Solanki, S. K., Barthol, P., Danilovic, S., et al. 2010, ApJL, 723, L127
Solanki, S. K., Inhester, B., & Schüssler, M. 2006, RPPh, 69, 563
Solanki, S. K., & Montavon, C. A. P. 1993, A&A, 275, 283
Solanki, S. K., & Steiner, O. 1990, A&A, 234, 519
Solanki, S. K., Riethmüller, T. L., Barthol, P., et al. 2017, ApJS, 229, 2
Solanki, S. K., Smitha, H. N., Lagg, A., et al. 2026, ApJL, 1005, L64
Yang, K. E., Tarr, L. A., Rempel, M., et al. 2024, ApJ, 976, 204